Upper Mantle Seismic Anisotropy as a Constraint for Mantle Flow and Continental Dynamics of the North American Plate

Wanying Wang[a,b,*], Thorsten W. Becker[a,b]

[a]*Institute for Geophysics, Jackson School of Geosciences, University of Texas at Austin, Austin, Texas, USA*

[b]*Department of Geological Sciences, Jackson School of Geosciences, University of Texas at Austin, Austin, Texas, USA*

Abstract

The alignment of intrinsically anisotropic olivine crystals under convection is typically invoked as the cause of the bulk of seismic anisotropy inferred from shear-wave splitting (SWS). This provides a means of constraining the interplay between continental dynamics and the deep mantle, in particular for densely instrumented regions such as North America after USArray. There, a comparison of "fast orientations" from SWS with absolute plate motions (APM) suggests that anisotropy is mainly controlled by plate motions. However, large regional misfits and the limited realism of the APM model motivate us to further explore SWS based anisotropy. If SWS is estimated from olivine alignment in mantle circulation instead, plate-driven flow alone produces anisotropy that has large misfits with SWS. The addition of large-scale mantle density anomalies and lateral viscosity variations significantly improves models. Although a strong continental craton is essential, varying its geometry does, however, not

*Corresponding author

Email address: wanying@utexas.edu (Wanying Wang)

improve the plate-scale misfit. Moreover, models based on higher resolution tomography degrade the fit, indicating issues with the flow model assumptions and/or a missing contributions to anisotropy. We thus compute a "lithospheric complement" to achieve a best-fit, joint representation of asthenospheric and frozen-in lithospheric anisotropy. The complement shows coherent structure and regional correlation with independently imaged crustal anisotropy. Dense SWS measurements therefore provide information on depth-dependent anisotropy with implications for tectonics, but much remains to be understood about continental anisotropy and its origin.

Keywords: continental dynamics, seismic anisotropy, North American plate

---

1. Introduction

Seismic anisotropy of the Earth's upper mantle is suggested to be mainly caused by the alignment of olivine aggregates in mantle flow. This is referred to as olivine lattice preferred orientation (LPO), and typical LPO is expected to align with shear under convection. This relationship provides a promising link between asthenospheric flow and seismic observations, in particular to study the relationships between surface geology and the underlying mantle dynamics in continental plates (e.g. Silver, 1996; Ismail and Mainprice, 1998; Long and Becker, 2010).

In order to obtain information about upper mantle flow, shear-wave splitting (SWS) analysis of teleseismic phases is widely used to infer upper mantle azimuthal anisotropy. SWS measures the separation of shear waves into two orthogonally polarized pulses upon traversing an anisotropic medium. The polarization plane orientation of the faster shear wave pulse is often called the "fast azimuth", and is expected to parallel the alignment of the seismically fast [100]-axes of the olivine aggregates and the sense of shear. The delay time between the fast and slow wave arrivals at the surface indicates the anisotropy magnitude accumulated along the path, and by inference, the depth extent or layer thickness of the anisotropic part of the mantle or lithosphere (e.g. Silver, 1996; Savage, 1999). Teleseismic SWS measurements use SKS, $SKKS$ and PKS phases that have nearly vertical ray paths and sample the upper mantle beneath the seismic stations with poor vertical, but good lateral resolution.

Recently, the USArray seismometer deployment during the EarthScope effort provided unprecedented coverage of United States, renewing efforts to investigate mantle dynamics within and underneath the North American plate (e.g. Hongsresawat et al., 2015; Long et al., 2016; Zhou et al., 2018). Here, we compare a range of mantle flow model predictions of upper mantle anisotropy to the observed SWS fast orientations to advance efforts of understanding North America upper mantle dynamics (Fig. 1).

The station-averaged SWS dataset used in this study is shown in Fig. 1b and newly spans the whole E-W extent of the continent at roughly uniform station spacing. The SWS compilation consists of 14,326 splits from the updated compilation of Becker et al. (2012), as well 29,061 standardized splits from Liu et al. (2014), Refayee et al. (2014), and Yang et al. (2016, 2017). We also include results from offshore experiments (Bodmer et al., 2015; Ramsay et al., 2015; Lynner and Bodmer, 2017).

As has been discussed earlier based on more limited compilations, the fast SWS orientation within the U.S. are generally E-W to NW-SE (e.g. Silver, 1996), exhibit a circular pattern beneath the Great Basin (e.g. Zandt and Humphreys, 2008; Hongsresawat et al., 2015), and orogen-parallel orientation beneath and around the Appalachians (e.g. Long et al., 2016) (Fig. 1). While we only further consider fast azimuths below, we note that the delay times of SWS are seen to vary in systematic fashion. Broadly speaking, delay times are larger beneath most of the western U.S. and the south central U.S., and delay times smaller beneath the interior plain, the

Appalachians and the southern Great Basin (Fig. 1).

In order to link those observations of azimuthal anisotropy at least geographically to continental dynamics, we can consider the geological history of the region. In the broadest of strokes, we note that the western U.S. has been tectonically active since the late Mesozoic, from the Laramide orogeny to the ongoing subduction-related orogenesis in the Cascades and extension in the Basin and Range. A relatively thinner lithosphere in the west likely plays a role in suggested scenarios where active mantle flow affects lithospheric deformation beneath the Basin and Range, the Colorado plateau and the Rockies (e.g. Savage and Sheehan, 2000; Karlstrom et al., 2012). Likewise, mantle flow itself may have eroded part of the lithosphere and caused thinning and extension at the Basin and Range (e.g. Lekić and Fischer, 2014). A thinner lithosphere relative to the cratonic eastern U.S. also implies a reduced role of possible shallow, frozen in anisotropy (e.g. Silver, 1996), and perhaps a more readily understandable link between asthenospheric flow and SWS.

The area through the central U.S. to the west of the Appalachian is within the extent of the North American Craton, which is part of the oldest lithosphere on Earth that had been stable for over 1.7 Ga (e.g. Hoffman, 1989). The lithospheric root beneath the craton extends to over 200 km depth (e.g. Gung et al., 2003; Steinberger and Becker, 2016), and is suggested to have higher viscosity than the surrounding mantle (e.g. Lenardic et al., 2003). Beneath the central U.S., the oldest part of the cratonic region

is stable since the Archean, and may preserve relatively larger degrees of shallow, frozen-in anisotropy. On the other hand, the cratonic root may divert upper mantle flow, perturbing flow at the cratons edge and inducing counter flow beneath it, which could possibly strengthen regional lithosphere-asthenosphere coupling (e.g. Silver, 1996; Fouch et al., 2000). This phenomenon is likely important for understanding the details of upper mantle flow dynamics and the origin of azimuthal anisotropy beneath the eastern U.S., which sits atop the cratonic boundary and edge.

Tectonic features in the eastern U.S. include the Proterozoic rifting and Paleozoic compressional orogenic events, followed by extensional events in the Mesozoic. Based on SWS splitting and modeling, Fouch et al. (2000) suggested that the observed anisotropy reveals the combined effect from the lithospheric and sublithospheric anisotropy in this region. Small-scale upper mantle density variations and lithospheric thickness variations exist in this region (Fig. 2) and might cause perturbations in anisotropy as well. For example, the northern Appalachian upwelling that can be inferred from slow seismic tomography anomalies (Schmandt and Lin, 2014) might relate to the Great Meteor hot spot track, and possibly indicate convection on relatively small scales in the surrounding mantle (e.g. Villemaire et al., 2012; Schmandt and Lin, 2014; Levin et al., 2018). Lithospheric thickness appears to decrease rapidly from the plateau to the east of the Appalachian, and is suggested to relate to lithospheric weakness from Eocene delamination (e.g. Mazza et al., 2014).

Convective flow models should be able to predict the current sublithospheric LPO to match the SWS observations if the models capture the major contributors that affect the present day upper mantle strain (e.g. Long and Becker, 2010). Given the extensive tectonic activity and prior sampling, much of the geodynamic SWS modeling previously focused on the western U.S.. For example, Silver and Holt (2002) jointly interpreted splitting and GPS observations to infer eastward mantle flow. Becker et al. (2006b) computed LPO from fluid mantle flow modeling, and showed that the western U.S. outside the Basin and Range domain could be fit well with relatively simple flow models as long as a downwelling associated with the Farallon slab was included. More recently, Zhou et al. (2018) computed anisotropy from more complex models with lateral viscosity variations (LVVs) and were able to reproduce the circular pattern discussed by Zandt and Humphreys (2008).

Given the long geological history of the North American plate, we expect that the lithosphere-asthenosphere system will reflect different contributions to anisotropy. Based on joint surface wave and SWS analysis, Yuan and Romanowicz (2010) suggested layering with various lithospheric azimuthal anisotropy orientations beneath North America, and many authors have made the case that variations in SWS fast orientations with back-azimuth are best explained by a significant lithospheric anisotropy source (Silver, 1996; Savage, 1999).

Here, we seek to address the azimuthal anisotropy signal underneath

all of the U.S., explore which role small-scale lateral variations in density and viscosity play for predictions of asthenospheric anisotropy, and then return to the question of the role of lithospheric anisotropy.

2. Methods

Mantle flow modeling

This study broadly follows the approach of Becker et al. (2006b) and Miller and Becker (2012). Under the Boussinesq and infinite Prandtl number approximations, the conservation equations for mass and momentum for purely viscous mantle flow are given by

$$\nabla \cdot u = 0,$$

$$-\nabla p + \nabla \cdot \eta(\nabla u + \nabla^T u)] - \delta\rho g \hat{e}_r = 0.$$

Here, u is the velocity vector, p is the dynamic pressure, η is the viscosity, $\delta\rho$ is the density anomaly, g is the gravitational acceleration and $\hat{e}_r$ is the radial unit vector. We solve the conservation equation using the finite element software CitcomS (Zhong et al., 2000) in a 3-D spherical domain. The surface boundary condition of most of our models are prescribed plate motions in the no-net-rotation (NNR) reference frame (NNR-NUVEL-1, by Argus and Gordon, 1991). The mechanical boundary condition at the core-mantle boundary is free-slip, and, therefore, the absolute reference frame

of the plate motions is irrelevant for relative velocities, and hence predictions of anisotropy.

Density variations outside continental cratons are assumed to be purely thermal and is scaled from seismic tomography anomalies $\ln v_S$ with a simplified scaling of $R = \frac{d \ln \rho}{d \ln V_S}$. Within cratons, where we expect compositional anomalies (e.g. Jordan, 1978), we assume the lithosphere to be neutrally buoyant and highly viscous by setting craton-related seismic velocity anomalies to zero in the upper 300 km depth, and prescribing compositional viscosities that are 500 times the ambient mantle value.

To ensure that the system is dynamically consistent, the resulting vigor of density-driven flow is adjusted via R such that when the same density variation is used in a model with free-slip surface boundary conditions, the same RMS surface velocity as for prescribed absolute plate motion (APM) results. The resulting $R = 0.24$ is in line with prior work (e.g. Miller and Becker, 2012). Inputs for the density variations of the flow models come from two tomography models: SMEAN is a composite, global S-wave tomography model (Becker and Boschi, 2002) used for reference (Fig. 2a). In order to capture the possible effect of small-scale density anomalies beneath the U.S. and advances in isotropic structural imaging thanks to USArray, we merge the regional tomography model of Schmandt and Lin (2014) with SMEAN to obtain a the fairly joint model MERGED where the edges of the embedded high resolution region are smoothed (Fig. 2b).

Both radial and lateral viscosity variations are considered in the flow computation. The viscosity inputs of the flow models is built upon a basic, three layered radial viscosity structure (RVV). The viscosity of each of the 0 – 100 km, 100 – 660 km, and 660 – 2891 km layers is 150, 1, and 60 times the reference value. For the 100 – 660 km depth range, a temperature dependent lateral viscosity variation (LVV) is applied to the three layered RVV structure, and the viscosity is given by equation: $\eta = \eta_0 \exp E(T - T_{ref})$. In this equation η_0 is from the RVV structure, E scales the effect of temperature dependence with a value of 7, T is the non-dimensional temperature at each point inferred from the tomography models, and T_{ref} is the non-dimensional reference temperature that equals to 0.5. In the upper 300 km, η is then multiplied by a structure dependent viscosity factor to account for the LVVs.

The viscosity factor at each of the plate boundaries, the oceanic and continental lithosphere, cratonic keels and oceanic asthenosphere is 0.01, 1, 50, 500, 0.01, respectively (cf. Miller and Becker, 2012). Focusing on continental keels underneath the U.S., we test two viscosity structures, models LVV1 and LVV2. The cratonic keel geometry of LVV1 is inferred from global tomography using the approach of Steinberger and Becker (2016) and the model SL2013 (Schaeffer and Lebedev, 2013). In LVV1, the minimum lithospheric thickness is 50 km in both continental and oceanic regions (Fig. 2c). LVV2 is taken from the reference craton model of Miller and Becker (2012) where keel geometry is simpler, and keel depth constant

at 300 km (Fig. 2d).

Asthenospheric and lithospheric anisotropy modeling

Based on the mantle circulation models, we then use particle tracking and the D-Rex mineral physics approximation (Kaminski et al., 2004) to compute LPO as the tracers are advected until a logarithmic saturation strain of 0.75 is reached (Becker et al., 2006b; Miller and Becker, 2012). We assume that mantle circulation is stationary over the few Myr that it takes to achieve this strain (cf. Becker et al., 2003, 2006a). Depth-dependent single crystal elasticity constants and Voigt averaging are then used to determine the elasticity tensor **C** at 25 km spaced locations underneath each of the stations where SWS is measured.

While SKS splitting is well known to not linearly average over **C** along the path, such differences are generally limited as long as anisotropy does not vary strongly with depth (e.g. Becker et al., 2006b, 2012). We conducted initial tests using the full-waveform approach of Becker et al. (2006b) and found that regionally, details of the SWS predictions were affected. However, our overall conclusions regarding the flow model predictions would be the same.

Here, we therefore only consider the simplified, depth-averaged tensor approach, computing an average for the 25 to 375 km depth range. Under the tensor-averaging assumption, the Christoffel equation is then solved for the equivalent SWS delay times and fast azimuths using a back-

azimuthal average. We leave the exploration of back-azimuthal dependence of SKS splitting for a future joint analysis with surface-wave inferred azimuthal anisotropy.

Upon having predicted the inferred LPO anisotropy caused by mantle flow in the asthenosphere, we compare it with the SWS observation and compute the absolute angular misfit, $\Delta\alpha$, between the two ($\Delta\alpha \in [0^\circ, 90^\circ]$) for a range of flow models. Given the relatively poor overall fit for the study area of those predictions compared to earlier work (e.g. Miller and Becker, 2012), we also explore the possible contributions of the lithosphere more extensively. For this, we perform an inversion for the best-fit thickness and azimuthal alignment of a hypothetical layer consisting of frozen-in anisotropy represented by a single elastic tensor. The inversion is based on a parameter space exploration and linear averaging of tensors, for simplicity. When the resulting, best-fit "lithospheric complement" is added to the asthenospheric anisotropy, SWS observations can be matched nearly perfectly. The tensors used here are an averaged single-crystal tensor with 70% olivine and 30% pyroxene from Estey and Douglas (1986) (Tensor 1), and an averaged tensor of the spreading type of xenolith dataset of Ismail and Mainprice (1998) (Tensor 2).

3. Results

SWS alignment with absolute plate motions

Assuming that plate motions at the surface in some absolute reference frame (APM) are reflective of the orientation of shear between the lithosphere and mantle, APM alignment is a first order test for the origin of anisotropy (Silver, 1996). The SWS fast orientation beneath the U.S. are indeed found to be generally aligned with plate motion directions (e.g. Hongsresawat et al., 2015). Figure 3 substantiates earlier analyses using our denser SWS dataset by comparing it with APM in the NNR reference frame (Argus and Gordon, 1991), and the spreading-aligned reference frame (Becker et al., 2015), for comparison.

On a plate scale, SWS fast axes have NE-SW orientations similar to the NNR APM orientation of North America, especially in the western U.S. (Fig. 3a), leading to a plate-scale mean misfit of $\langle \Delta\alpha \rangle \approx 30^\circ$. The spreading-aligned APM is more similar to the SWS fast orientations and $\langle \Delta\alpha \rangle$ is further reduced by $\sim 5^\circ$ (Fig. 3b). While misfit values thus depend on different APM reference frames (e.g. Becker et al., 2015), similar local misfit fluctuations are observed, and those may be related to mantle flow deviating from implied APM shear. For example, in the southeastern Rockies, the large angular misfit might relate to local lithospheric thickness variations (Refayee et al., 2014; Hongsresawat et al., 2015). Another significant misfit is found at the eastern U.S. margin and the southern Appalachian Mountains, where azimuthal anisotropy possibly contains a

lithospheric frozen-in component (e.g. Levin et al., 2018; Long et al., 2016).

Flow model predictions for SWS

We now test the role of asthenospheric convection patterns other than APM shearing by predicting anisotropy from the sublithospheric flow that is driven by plate motion alone, or in addition by density variations. We investigate the effect of viscosity variations caused by cratons, a weak oceanic asthenosphere layer, and plate boundary weak zones. For each flow model, we explore the flow itself, and compute the misfit between predicted and observed anisotropy, $\Delta\alpha$. While mantle flow is resolved globally and on scales of 25 km (Miller and Becker, 2012), we find it helpful to visualize the effect of shearing in flow models by plotting the vector difference $\vec{v}_{shear}$ between the horizontal flow velocities at the surface $\vec{v}_{surface}$ and at a typical, 200 km depth $\vec{v}_{200km}$ with

$$\vec{v}_{shear} = \vec{v}_{200km} - \vec{v}_{surface},$$

as such differential velocities can be a rough proxy for LPO alignment.

The effect of plate motion induced circulation with LVVs

Our starting Model 1 only has radial viscosity variations and is purely driven by the prescribed boundary condition of APM motion at the surface. Given the effects of plate geometry and return flow, we expect that the induced asthenospheric shearing will be different from the APM

model of Fig. 3 even for this simple circulation model (e.g. Long and Becker, 2010), and this is indeed the case.

Figure 4a shows that beneath the western and central U.S., the direction of $\vec{v}_{200km}$ deviates from the plate motion direction due to the flow perturbation at the Pacific-North America plate boundary. The flow direction is to the W to SW and the shear direction forms an 110° to 150° angle with the plate motion in this region. While the details will depend on the viscosity structure (cf. Becker et al., 2006b), this plate boundary flow perturbation extends almost throughout half the continents for our reference model. In the Eastern U.S., sublithospheric Couette flow (Fig. 5a) is more in line with APM, such that shear is roughly into the opposite direction (Fig. 4a). The mis-alignment of shear and plate motion vectors is subdued in the eastern U.S. but still of order 20° to 30°.

Since there are no small-scale flow perturbation or abrupt changes in viscosity, the orientation of differential velocities of Fig. 4a are representative of the predicted anisotropy (Fig. 4b). W-E oriented predicted fast axes fit well with the SWS observation onshore in NW U.S.. However, there are large misfits with regions of consistent $\sim 90^\circ$ misalignment such as the in the southern Rockies. The overall match between SWS and predictions is very poor at $\langle \Delta\alpha \rangle \approx 45^\circ$ (which is the expectation for two random orientational fields). This indicates that plate-induced shear flow, the presumably more realistic version of the assumption behind APM alignment, is actually a much worse model in this case compared to the APM hypothesis of

Fig. 3.

Based on Model 1, Model 2 adds in weak plate boundaries and strong cratonic keels from viscosity model LVV1. Comparing Models 1 and 2, changes in horizontal flow mainly occur beneath and around the craton (Figs. 4a and c). The spatial extent of this change is shown in the differential flow velocity profile in Fig. 5d. Due to its high viscosity, the craton maintains and enhances plate-like motion down to ~ 300 km depth, as shown in Fig. 4c, and transfers it to the sublithospheric mantle. The craton also causes minor flow perturbations in the radial direction at the lithospheric thickness discontinuities beneath the Colorado Plateau (Fig. 5d). However, the directional change in flow introduced by the keel is overall small, such that the anisotropy predictions of Models 1 and 2 are fairly similar (Figs. 4b and d). The weak plate boundary effect of Model 2 changes the flow and shear direction beneath the Juan de Fuca Plate, for example, slightly reducing $\Delta\alpha$ there (Fig. 4d).

Model 3 adds in a 200 km thick oceanic asthenosphere that is 100 times weaker than the ambient mantle compared to Model 2 (cf. Becker, 2017). Comparing the flow fields in Models 2 and 3, we see significant differences in flow pattern beneath the oceanic plates and adjacent areas (Figs. 4c and e). Differential velocities, $\vec{v}_{200km}$, and the APM within the oceanic region are nearly parallel in Model 2 (Fig. 4c), while in Model 3 they are perpendicular within the Pacific and form 40° to 60° angles within the Atlantic domain (Fig. 4e). The flow modification leads to a rotation in predicted ani-

sotropy orientations from NW-SE in Model 2 to W-E in Model 3 (Figs. 4b and d).

Angular misfits $\Delta\alpha$ in Model 3 are reduced to $< 10^\circ$ in parts of the western and eastern U.S. (Fig. 4f). This region of anisotropy modification is approximately where the thickest part of the craton is located in our model (Fig. 2c). Here, a weak sub-oceanic asthenosphere helps to create APM parallel flow and shear beneath the craton (cf. Miller and Becker, 2012). However, at greater depth the flow changes to westward, so the depth-averaged shear vector and predicted fast axes orient approximately W-E instead of parallel to the plate motion. Overall, the weak asthenosphere in plate-driven flow models accommodates the lithospheric shear beneath the PA plate, slows down the westward sublithospheric flow motion beneath the U.S., and amplifies return flow at 400 km depth (Figs. 5c and e). The misfit is overall reduced to $\langle\Delta\alpha\rangle \approx 36^\circ$ for Model 3. These tests suggests that a sub-oceanic viscosity reduction, as a much larger-scale feature compared to plate boundaries and continental cratons, can have a major control over the plate-driven shear (cf. Conrad and Lithgow-Bertelloni, 2006).

The effect of density driven flow

We next investigate the effect of density-driven flow by adding anomalies inferred from SMEAN and MERGED tomography models to Model 2, resulting in Models 4 and 5, respectively. The direction of $\vec{v}_{200km}$ in Model 4

changes nearly 180° from the western to central U.S. (Fig. 6a) relative to Model 2, also clearly seen in the flow profile of Fig. 7a. This flow patterns results from an upwelling underneath the western U.S. and a lower-mantle, Farallon-related slab sinker anomaly. Those were earlier shown to lead to strong, APM opposite counter flow underneath the western half of the U.S. (e.g. Becker et al., 2006b), and are here seen to be further modulated by the cratonic keel.

Density anomalies from SMEAN as incorporated in Model 4 result in shear and predicted anisotropy fast axes oriented W-E to WSW-ENE beneath the north western U.S. and west central U.S., W-E to WNW-ESE beneath the east central U.S. and north eastern U.S., and SW-NE beneath the south eastern U.S. (Figs. 6a and b). In these regions, the predicted anisotropy fits the SWS observation nearly as well as the APM model (Fig. 3), and the overall misfit is $\langle \Delta\alpha \rangle \approx 32^\circ$. This substantiates that a contribution of density-induced flow to plate-driven shear is needed for an appropriate prediction of LPO anisotropy, and hence a realistic mantle circulation estimate, as has been argued for global models (e.g. Behn et al., 2004; Becker et al., 2015).

The flow pattern and predicted anisotropy orientation in Model 5 based on MERGED are overall similar to Model 4 (Figs. 6c, d and Fig. 7b), but have, expectedly, more small-scale perturbations due to the higher resolution, regional tomography model of Schmandt and Lin (2014). Those features include the radial flow beneath Yellowstone and Snake River

Plain (e.g. Savage and Sheehan, 2000), Salton Trough, northern Great Valley, Rio Grande Rift, New England and central Appalachian, as outlined in Fig. 2b. Some of these smaller-scale flow structures inferred from MERGED affect the predicted anisotropy significantly. For example, beneath the northern Great Valley, which corresponds to a $\sim 5^\circ \times 5^\circ$ region with large $\Delta\alpha$ in Model 4, the dense structure that is suggested to be a volcanic drip (Zandt et al., 2004) changes the predicted anisotropy orientation from nearly N-S in Model 4 to either SW-NE or NW-SE in Model 5, and results in a $\sim 45^\circ$ improvement in $\Delta\alpha$ values locally.

However, on balance, a degradation of the fit to SWS results on the scale of the whole U.S. is seen when the presumably better resolved MERGED tomography is used, with mean misfit increased to $\langle\Delta\alpha\rangle \approx 38^\circ$ (Fig. 6d). This means that asthenospheric flow is sensitively and diagnostically mapped into SWS predictions, but simply adding newer density models to existing flow computations does not provide a more consistent description of mantle dynamics. In fact, the opposite is true.

The effect of different LVVs in density and plate-driven flow models

LVVs were seen to improve the fit of purely plate-driven flow to SWS observations (cf. Figs. 4b and f). Adding density-driven flow on large scales further improved the fit to observation to a level that is comparable to the APM model (Fig. 6b), but not for the smaller-scale anomalies of MERGED (Fig. 6d). We therefore explore the other major contribution to

flow besides density, viscosity variations, further.

To complement the tests of Figs. 4 and 6 and focus on LVVs specifically, we explore six additional models (Figs. 8 and 9). For the tomography model SMEAN, we build a new reference, Model 6, by prescribing density variations to Model 1. We then build Models 7 and 8 by prescribing LVV models LVV1 and LVV2 to Model 6. Model 7 is different from Model 4 because it has the oceanic asthenosphere to allow for full investigation of the LVVs and also to help to distinguish the effect of the craton from the oceanic asthenosphere when comparing to Model 4. Similarly, for tomography model MERGED, we have Model 9 in which there are no LVVs, and Models 10 and 11 that use LVV1 and LVV2.

Without LVVs, the anisotropy predicted by Model 6 has W-E orientation beneath the north western U.S. and west central U.S. and fits the observed SWS regionally quite well (Fig. 8a). Other regions have very large angular misfits, raising the average to $\langle \Delta\alpha \rangle \approx 50^\circ$, worse than for pure plate-driven shear (Fig. 4b). Model 9 shows similar patterns (Fig. 8d), besides the southeastern edge of the western U.S., for example.

Comparing Model 7 to 6 (Figs. 8a and b) and Model 10 to 9 (Figs. 8d and e), we see that prescribing LVVs in flow models degrades the fit offshore the east coast, improves the fit between predicted and observed anisotropy in the central and eastern U.S., and largely modifies, although does not improve, the predicted anisotropy in the western U.S. (overall drop in $\langle \Delta\alpha \rangle$ is $\approx 6^\circ$ compared to no LVVs). The effects of craton flow

modification (Figs. 9b and e) affect regional misfits but do not lead to an overall improvement compared to the best flow model of Fig. 6b. Changing the viscosity structure to the LVV2 models leads to better coupled flow with the plate motion beneath the craton and thus changes the predicted anisotropy orientation in the northern part of the central and eastern U.S. (Figs. 8-c and f). LVV1 and LVV2 have different keel shapes (Figs. 2c and d) and deflect or lead the flow differently. Indeed, comparing the regionally broken down mean misfits of Fig. 8b and c, as well as e and f, we can see changes particularly for the MERGED model. However, these effects of anisotropy modification are not overall beneficial, and the mean misfit values for models with the two viscosity structures are comparable.

Comparing flow profile residuals of the SMEAN flow models (Figs. 9b and c), they both show better coupled sublithospheric flow velocity beneath the craton to the plate motion. The craton slows down the eastward flow beneath the western U.S., and speeds up the westward flow beneath the eastern U.S., relative to simpler viscosity models. For SMEAN, LVV1 causes more perturbations on the radial direction to the flow beneath it, while LVV2 mainly leads the sublithospheric flow horizontally. The MERGED flow models have similar residual flow pattern overall, but see more variations in magnitude and direction upon adding the cratons (Figs. 9e and f), suggesting that the LVVs can amplify the density variation effects, as was seen in the larger effect on the regional mean misfit values.

In summary, we find that the effects of different assumptions on as-

thenospheric density anomalies lead to the largest differences in predicted anisotropy. Yet, presumably higher resolution tomography does not improve the fit to SWS observations. Lateral viscosity variations help improve the fit when cratons and sub-oceanic viscosity reductions are introduced. Modifying the keel geometries between models LVV1 and LVV2 does improve the fit to SWS locally, but none of the modified LVV models we considered can make up for the degradation of fit observed for MERGED compared to SMEAN density anomalies.

4. Discussion

Sensitivity of mantle flow modeling

We confirm that lateral viscosity variations can play an important role in controlling upper mantle flow underneath continental regions (e.g. Fouch et al., 2000; Miller and Becker, 2012). Plate-motion induced mantle-flow model predictions of SWS observations of azimuthal anisotropy are much improved when LVVs are added (Figs. 4b and f). This improvement is mainly due to the implementation of a strong cratonic keel and a weak oceanic asthenosphere which lead to enhancement and reduction of the coupling between plate motions and sublithospheric mantle, respectively (e.g. Conrad and Lithgow-Bertelloni, 2006; Becker, 2017). However, for purely plate-driven flow, the addition of a stiff craton does not cause significant regional flow deflection in lateral or radial directions, unlike what might be expected given experiments using simpler geometries (e.g.

Fouch et al., 2000). Moreover, the fit to SWS of plate-driven flow is worse than the likely unphysical assumption of alignment with APM motions.

In models that also include the effect of mantle density anomalies for flow, in contrast, the craton amplifies the small-scale radial flow and causes more significant lateral deflection and strong downward deflection on scales that are relevant for regional anisotropy. In conjunction, the effects of density-driven flow and lateral viscosity variations are reflected in anisotropy, and SWS observations therefore do appear diagnostic of both density and viscosity anomalies on scales of 100s of km.

SWS and flow dynamic studies have, of course, long suggested the importance of density anomalies for North American plate dynamics, for example related to the Juan de Fuca and Farallon slabs (e.g. Becker et al., 2006b; Zandt and Humphreys, 2008), possible mantle drips (e.g. West et al., 2009) and mantle upwellings (e.g. Savage and Sheehan, 2000). Such anomalies should be better captured by the MERGED model based on regionally improved tomography, which makes it interesting that the addition of smaller-scale mantle structure actually leads to a worsening of the misfit between model predictions and azimuthal anisotropy observations (Figs. 6b and d). This is perhaps the most significant finding of our study, and was unexpected given prior successes of the general modeling approach.

Let us assume that structural models from seismology have in fact improved thanks to USArray, and that the most fundamental assumptions

for our approach hold, i.e. that upper mantle anisotropy is at least partially caused by LPO alignment under asthenospheric mantle flow, and that mantle flow can be estimated with mantle circulation models that have been validated with a range of other datasets (e.g. Long and Becker, 2010). There are then several possible, not mutually exclusive nor exhaustive reasons for why our best circulation-based model is one that is based on plate-driven flow, the SMEAN large-scale mantle density anomalies, and simple LVVs.

First, given the sensitivity of LPO predictions to details of the LVVs, different keel structures, non-linear rheology, variations in volatile content, or additional compositional dependence of viscosity may all lead to lateral viscosity variations that counterbalance the detrimental effects of adding small-scale density structure of MERGED. A formal inversion for these variations may be possible, but none of our forward tests (most not shown) trying different LVV structures have led to plate-scale improvement in mean misfit. Figure 8 illustrates the sorts of variations in LPO predictions one might expect. These effects are in line with arguments about local effects, e.g. of drips and the like, but we leave the exploration of more complex mantle LVV models that could possibly reconcile the predictions for later study. The general applicability of such optimized models will also be questionable should the LVVs not be based on some additional, general physical relationship not explored here.

Second, our scaling between seismic tomography and density anoma-

lies might be wrong, and this is clearly the case in principle, given the highly simplified nature of our linear, depth-independent scaling. Besides temperature, other properties, especially compositional heterogeneity and anelasticity, can also affect seismic wave velocity (e.g. Forte and Perry, 2000; Cammarano et al., 2003). In particular, we expect that cratonic regions of the continental lithosphere may be neutrally buoyant ("isopycnic", Jordan, 1978) which is why we corrected for this effect in a coarse fashion in our mantle flow models. The isopycnic assumption is not expected to be perfectly true at all depths, nor is the extent of cratons or the thickness of the lithosphere well constrained (e.g. Lekić and Fischer, 2014; Steinberger and Becker, 2016). We therefore cannot rule out that more sophisticated models including a wider range of compositional anomalies would lead to better predictions of LPO based anisotropy using the high resolution tomography models such as MERGED.

However, we conducted a range of tests where we varied the R scaling step wise from zero to 100% its reference value, and found that the signal inherent in MERGED leads to a degradation of the fit compared to SMEAN as soon as the density effects are felt by mantle flow. This would seem to imply that compositional anomalies would have to cancel out much of the signal seen in MERGED compared to SMEAN to at least not degrade the fit. This is possible, but would also question the general interpretations of seismic tomography for regional tectonics.

Third, time-dependence of mantle convection, and in particular

changes in plate motions, may complicate the interpretation of LPO based anisotropy even for the relatively short time-scales needed to saturate fabrics within the asthenosphere (e.g. Kaminski et al., 2004; Becker et al., 2006a). On global scales, Becker et al. (2003) showed that this effect was detectable, but seismological models did not allow determining which models were better within the margin given imperfect resolution.

Regionally, the story may be different, and Zhou et al. (2018) explored such effects for the western U.S. recently in detail. The authors pointed out the importance of the Juan de Fuca slab and a hot mantle anomaly beneath the western U.S. for the formation of the circular anisotropy pattern beneath the Great Basin. However, the anisotropy adjacent to that pattern was not as well fit, implying similarly mixed results in terms of a comprehensive explanation of SWS observations within the continental U.S..

There are thus at least three plausible reasons why a purely asthenospheric origin of anisotropy appears to be a moderately successful explanation of the large-scale SWS signal for the U.S. at best. In the remainder, we will instead assume, for the sake of argument, that our computations are in fact very good predictions of asthenospheric anisotropy, so good that we can ask about a missing lithospheric component needed to fit SWS observations.

The lithospheric complement

A lithospheric, frozen-in origin of anisotropy has long been discussed for the shallow oceanic lithosphere, as well as the bulk of the thicker and petrologically more heterogeneous continental lithosphere (e.g. Silver, 1996). Assuming that the difference between the SWS observations and flow predictions of LPO anisotropy arises entirely from the lithospheric component, we can augment a flow model with its corresponding lithospheric complement that would be needed to achieve a (near) perfect fit to SKS splitting, under the assumptions of our inversion such as depth-constant averaging along a vertical ray path underneath the station.

Figure 10 shows results for the lithospheric complements for the best performing LPO based on flow models, Models 4 (SMEAN) and 5 (MERGED). We first use a single crystal, composite olivine/pyroxene elastic tensor, Tensor 1 (Estey and Douglas, 1986), to conduct this experiment. We do, of course, not expect the lithosphere to consist of a uniformly aligned mixture of olivine and orthopyroxene, but this tensor may serve to illustrate the general behavior. In computing results for Figure 10, we allow for dip variations of the lithospheric tensor, and the misfits for the resulting SWS observation for the optimized two layer case are $\Delta\alpha \lesssim 2^{\circ}$. We can also maintain the best-fit hexagonal symmetry axis in the horizontal plane. In this case, the lithospheric complement would display similar orientations, but with ~ 20 km reduction in the hypothetical layer thickness, since the non-dipping tensor leads to higher anisotropy magnitude.

The resulting $\Delta\alpha$ are increased by $\sim 2^{\circ}$, which would still be within the typical "error", or rather back-azimuthal and filtering dependent variations, of SWS estimates.

As Figs. 10a and b show, the thickness of this hypothetical layer of Tensor 1 is typically of order ~ 75 km or so, meaning that an even thicker lithosphere of reduced local anisotropy strength might actually be physically plausible, at least for parts of North America. Perhaps more importantly, we find that the patterns of the best fit alignment of the lithospheric complement are fairly smooth over much of the study area. This might be expected from the spatial heterogeneity of SWS and seismic tomography, but implies that there could be a relation with a deterministic tectonic or convective process. The lithospheric complement is different for the two flow models in detail, but there are also consistent features. That said, the connection of the lithospheric complement's azimuthal alignment patterns to geological history is not immediately apparent, at least to us.

However, we can check if the features of the complement are at least consistent with other possibly related observations. To this end, we visually compare the complements with an azimuthal anisotropy model inferred from 16 s period Rayleigh wave H/V ratio by Lin and Schmandt (2014) (Fig. 10e). While those Rayleigh waves are mainly sensitive to the uppermost crustal layers, the anisotropy orientations appear related to tectonic regions that are important for continental dynamics, such as the Great Basin, the Rockies and the Precambrian Rift Margin (Lin and

Schmandt, 2014). Without going to details of the relationship between crustal anisotropy and tectonics, we note that there are fairly good correlations in orientations between our fitted lithospheric complement and the crustal anisotropy along the west coast of the U.S., beneath the Columbia Plateau, the southern Basin and Range, south of the Colorado plateau, Texas and the southern Coastal Plain (Figs. 10a and b). Beneath the eastern U.S., Model 5's lithospheric complement matches the crustal model while Model 4's does not.

To further explore this approach, we also consider Tensor 2 which is from xenolith samples inferred to be from spreading centers (Ismail and Mainprice, 1998), and presumably more realistic in terms of anisotropy strength. Throughout the study area in Figs. 10c and d, Tensor 2's lithospheric complement orientation is similar to Tensor 1, as expected, while the hypothetical layer thickness is ~ 50 km thicker reflecting relatively small anisotropy amplitude of Tensor 2 compared to Tensor 1 (e.g. Fig. B1 of Becker et al., 2006a).

The resulting layer thickness of the lithospheric complement for both tensors is relatively small with the central U.S., where the misfit between flow predicted anisotropy and the SWS observation is small in Figs. 6b and d, and thicker in the western and eastern U.S., where $\Delta\alpha$ is larger. Given that the lithosphere itself is relatively thin in the western U.S., the lithospheric complement may mask other effects leading to our asthenospheric flow predictions to fail in matching SWS in the west, but could

actually reflect frozen-in structures in the east. Good correlation of the crustal anisotropy model and the lithospheric complement in the eastern U.S. indicates the possibility that MERGED predicts the sublithospheric anisotropy better than SMEAN even if the asthenospheric LPO alone leads to a poor fit. This further suggests the importance of understanding lithospheric anisotropy, which would help to resolve the connection between small-scale mantle structures and the upper mantle anisotropy formation and SWS observation.

These findings substantiate that new insights into continental dynamics may yet be revealed by modeling anisotropy due to mantle flow, but the answer might at least regionally have to involve more detailed study of the lithospheric origin and longer-term geological history. Such future work should be especially promising once noise and ballistic surface wave inferences for crustal and mantle anisotropy are adequately incorporated.

5. Conclusions

Azimuthal anisotropy in the upper mantle as seen by shear wave splitting throughout the U.S. and offshore portions of the North American plate can be modeled by mantle circulation models. These models allow exploring the effect of density anomalies and viscosity variations within the asthenosphere, which strongly affect predictions of flow-based anisotropy when acting together. Large-scale flow models lead to misfits that are comparable to the absolute plate motion alignment hypothesis for

the study region. This confirms the general validity of the approach, but smaller-scale density anomalies of modern, EarthScope era tomography degrade the fit, and none of the viscosity models we considered can make up for it. "Lithospheric complements" can be estimated from the best flow model based anisotropy, and those match independent estimates of crustal anisotropy. This indicates promising avenues forward, but much is still to be learned about the link between seismic anisotropy and mantle flow and continental dynamics.

6. Acknowledgments

WW and TWB were partially supported by NSF EAR-1460479. All figures were prepared with the Generic Mapping Tools. We thank B. Schmandt and F. Lin for sharing their tomography and crustal anisotropy models with us. We thank our collaborators, K. Liu and S. Gao, for sharing their SWS dataset with us. We also thank L. Fuchs and R. Porritt at the Geodynamics group at the Jackson School of Geosciences for help and discussions.

674 Argus, D. F., Gordon, R. G., 1991. No-net-rotation model of current plate
675 velocities incorporating plate motion model NUVEL-1. Geophys. Res.
676 Lett. 18 (11), 2039–2042.

677 Becker, T. W., 2017. Superweak asthenosphere in light of upper-mantle
678 seismic anisotropy. Geochem., Geophys., Geosys. 18, 1986–2003.

679 Becker, T. W., Boschi, L., 2002. A comparison of tomographic and geody-
680 namic mantle models. Geochem., Geophys., Geosys. 3 (1).

681 Becker, T. W., Chevrot, S., Schulte-Pelkum, V., Blackman, D. K., 2006a. Sta-
682 tistical properties of seismic anisotropy predicted by upper mantle geo-
683 dynamic models. J. Geophys. Res. 111 (B8), B08309.

684 Becker, T. W., Kellogg, J. B., Ekström, G., O'Connell, R. J., 2003. Compari-
685 son of azimuthal seismic anisotropy from surface waves and finite strain
686 from global mantle-circulation models. Geophys. J. Int. 155 (2), 696–714.

687 Becker, T. W., Lebedev, S., Long, M. D., 2012. On the relationship between
688 azimuthal anisotropy from shear wave splitting and surface wave to-
689 mography. J. Geophys. Res. Solid Earth 117 (B1).

690 Becker, T. W., Schaeffer, A. J., Lebedev, S., Conrad, C. P., 2015. Toward
691 a generalized plate motion reference frame. Geophys. Res. Lett. 42 (9),
692 3188–3196.

693 Becker, T. W., Schulte-Pelkum, V., Blackman, D. K., Kellogg, J. B.,

694 O'Connell, R. J., 2006b. Mantle flow under the western United States
695 from shear wave splitting. Earth Planet. Sci. Lett. 247 (3-4), 235–251.

696 Behn, M. D., Conrad, C. P., Silver, P. G., 2004. Detection of upper mantle
697 flow associated with the African Superplume. Earth Planet. Sci. Lett.
698 224, 259–274.

699 Bodmer, M., Toomey, D. R., Hooft, E. E., Braunmiller, J., 2015. Seismic ani-
700 sotropy beneath the Juan de Fuca plate system: Evidence for heteroge-
701 neous mantle flow. Geology 43.

702 Cammarano, F., Goes, S., Vacher, P., Giardini, D., 2003. Inferring upper-
703 mantle temperatures from seismic velocities. Phys. Earth Planet. Inter.
704 138 (3-4), 197–222.

705 Conrad, C. P., Lithgow-Bertelloni, C., 2006. Influence of continental roots
706 and asthenosphere on plate-mantle coupling. Geophys. Res. Lett. 33 (5),
707 L05312.

708 Estey, L. H., Douglas, B. J., 1986. Upper mantle anisotropy: A preliminary
709 model. J. Geophys. Res. 91 (B11), 11393.

710 Forte, A. M., Perry, H. K., 2000. Geodynamic evidence for a chemically
711 depleted continental tectosphere. Science 290 (5498), 1940–1944.

712 Fouch, M. J., Fischer, K. M., Parmentier, E. M., Wysession, M. E., Clarke,
713 T. J., 2000. Shear wave splitting, continental keels, and patterns of mantle
714 flow. J. Geophys. Res. Solid Earth 105 (B3), 6255–6275.

715 Gung, Y., Panning, M., Romanowicz, B., 2003. Global anisotropy and the
716 thickness of continents. Nature 422 (6933), 707–711.

717 Hoffman, P. F., 1989. Speculations on Laurentia's first gigayear (2.0 to 1.0
718 Ga). Geology 17 (2), 135.

719 Hongsresawat, S., Panning, M. P., Russo, R. M., Foster, D. A., Monteiller,
720 V., Chevrot, S., 2015. USArray shear wave splitting shows seismic aniso-
721 tropy from both lithosphere and asthenosphere. Geology 43 (8), 667–670.

722 Ismail, W. B., Mainprice, D., 1998. An olivine fabric database: an overview
723 of upper mantle fabrics and seismic anisotropy. Tectonophysics 296 (1-
724 2), 145–157.

725 Jordan, T. H., 1978. Composition and development of the continental tec-
726 tosphere. Nature 274 (5671), 544–548.

727 Kaminski, E., Ribe, N. M., Browaeys, J. T., 2004. D-Rex, a program for cal-
728 culation of seismic anisotropy due to crystal lattice preferred orientation
729 in the convective upper mantlé mantlé. Geophys. J. Int 158, 744–752.

730 Karlstrom, K. E., Coblentz, D., Dueker, K., Ouimet, W., Kirby, E., Van Wijk,
731 J., Schmandt, B., Kelley, S., Lazear, G., Crossey, L. J., Crow, R., Aslan, A.,
732 Darling, A., Aster, R., MacCarthy, J., Hansen, S. M., Stachnik, J., Stockli,
733 D. F., Garcia, R. V., Hoffman, M., McKeon, R., Feldman, J., Heizler, M.,
734 Donahue, M. S., 2012. Mantle-driven dynamic uplift of the Rocky Moun-

735 tains and Colorado Plateau and its surface response: Toward a unified
736 hypothesis. Lithosphere 4, 3–22.

737 Lekić, V., Fischer, K. M., 2014. Contrasting lithospheric signatures across
738 the western United States revealed by Sp receiver functions. Earth
739 Planet. Sci. Lett. 402, 90–98.

740 Lenardic, A., Moresi, L.-N., Mühlhaus, H., 2003. Longevity and stabil-
741 ity of cratonic lithosphere: Insights from numerical simulations of cou-
742 pled mantle convection and continental tectonics. J. Geophys. Res. Solid
743 Earth 108 (B6).

744 Levin, V., Long, M. D., Skryzalin, P., Li, Y., López, I., 2018. Seismic evidence
745 for a recently formed mantle upwelling beneath New England. Geology
746 46 (1), 87–90.

747 Lin, F.-C., Schmandt, B., 2014. Upper crustal azimuthal anisotropy across
748 the contiguous U.S. determined by Rayleigh wave ellipticity. Geophys.
749 Res. Lett. 41 (23), 8301–8307.

750 Liu, K. H., Elsheikh, A., Lemnifi, A., Purevsuren, U., Ray, M., Refayee, H.,
751 Yang, B. B., Yu, Y., Gao, S. S., 2014. A uniform database of teleseismic
752 shear wave splitting measurements for the western and central United
753 States. Geochemistry, Geophysics, Geosystems 15 (5), 2075–2085.

754 Long, M. D., Becker, T. W., 2010. Mantle dynamics and seismic anisotropy.
755 Earth Planet. Sci. Lett. 297 (3-4), 341–354.

Long, M. D., Jackson, K. G., McNamara, J. F., 2016. SKS splitting beneath Transportable Array stations in eastern North America and the signature of past lithospheric deformation. Geochemistry, Geophysics, Geosystems 17 (1), 2–15.

Lynner, C., Bodmer, M., 2017. Mantle flow along the eastern North American margin inferred from shear wave splitting. Geology 45 (10), 867–870.

Mazza, S. E., Gazel, E., Johnson, E. A., Kunk, M. J., McAleer, R., Spotila, J. A., Bizimis, M., Coleman, D. S., 2014. Volcanoes of the passive margin: The youngest magmatic event in eastern North America. Geology 42 (6), 483–486.

Miller, M. S., Becker, T. W., 2012. Mantle flow deflected by interactions between subducted slabs and cratonic keels. Nat. Geosci. 5 (10), 726–730.

Ramsay, J., Kohler, M. D., Davis, P. M., Wang, X., Holt, W., Weeraratne, D. S., 2015. North America plate boundary offshore southern California. Geophys. J. Int. 207.

Refayee, H. A., Yang, B. B., Liu, K. H., Gao, S. S., 2014. Mantle flow and lithosphereasthenosphere coupling beneath the southwestern edge of the North American craton: Constraints from shear-wave splitting measurements. Earth Planet. Sci. Lett. 402, 209–220.

776 Savage, M. K., 1999. Seismic anisotropy and mantle deformation: What
777 have we learned from shear wave splitting? Rev. Geophys. 37, 65–106.

778 Savage, M. K., Sheehan, A. F., 2000. Seismic anisotropy and mantle flow
779 from the Great Basin to the Great Plains, western United States. J. Geo-
780 phys. Res. Solid Earth 105 (B6), 13715–13734.

781 Schaeffer, A. J., Lebedev, S., 2013. Global shear speed structure of the upper
782 mantle and transition zone. Geophys. J. Int. 194 (1), 417–449.

783 Schmandt, B., Lin, F.-C., 2014. P and S wave tomography of the mantle
784 beneath the United States. Geophys. Res. Lett. 41 (18), 6342–6349.

785 Silver, P. G., 1996. Seismic anisotropy beneath the continents: Probing the
786 depths of geology. Annu. Rev. Earth Planet. Sci 24, 385–432.

787 Silver, P. G., Holt, W. E., 2002. The mantle flow field beneath Western North
788 America. Science 295, 1054–1057.

789 Steinberger, B., Becker, T. W., 2016. A comparison of lithospheric thickness
790 models. Tectonophysics.

791 Villemaire, M., Darbyshire, F. A., Bastow, I. D., 2012. P-wave tomography
792 of eastern North America: Evidence for mantle evolution from Archean
793 to Phanerozoic, and modification during subsequent hot spot tectonism.
794 J. Geophys. Res. Solid Earth 117 (B12).

795 West, J. D., Fouch, M. J., Roth, J. B., Elkins-Tanton, L. T., 2009. Vertical
796 mantle flow associated with a lithospheric drip beneath the Great Basin.
797 Nat. Geosci. 2 (6), 439–444.

798 Yang, B. B., Liu, K. H., Dahm, H. H., Gao, S. S., 2016. A Uniform Database
799 of Teleseismic ShearWave Splitting Measurements for the Western and
800 Central United States: December 2014 Update. Seismol. Res. Lett.
801 87 (2A), 295–300.

802 Yang, B. B., Liu, Y., Dahm, H., Liu, K. H., Gao, S. S., 2017. Seismic az-
803 imuthal anisotropy beneath the eastern United States and its geody-
804 namic implications. Geophys. Res. Lett. 44 (6), 2670–2678.

805 Yuan, H., Romanowicz, B., 2010. Lithospheric layering in the North Amer-
806 ican craton. Nature 466 (7310), 1063–1068.

807 Zandt, G., Gilbert, H., Owens, T. J., Ducea, M., Saleeby, J., Jones, C. H.,
808 2004. Active foundering of a continental arc root beneath the southern
809 Sierra Nevada in California. Nature 431 (7004), 41–46.

810 Zandt, G., Humphreys, E., 2008. Toroidal mantle flow through the western
811 U.S. slab window. Geology 36 (4), 295.

812 Zhong, S., Zuber, M. T., Moresi, L. N., Gurnis, M., 2000. Role of
813 temperature-dependent viscosity and surface plates in spherical shell
814 models of mantle convection. J. Geophys. Res. 105, 11063–11082.

Zhou, Q., Hu, J., Liu, L., Chaparro, T., Stegman, D. R., Faccenda, M., 2018. Western U.S. seismic anisotropy revealing complex mantle dynamics. Earth Planet. Sci. Lett. 500, 156–167.

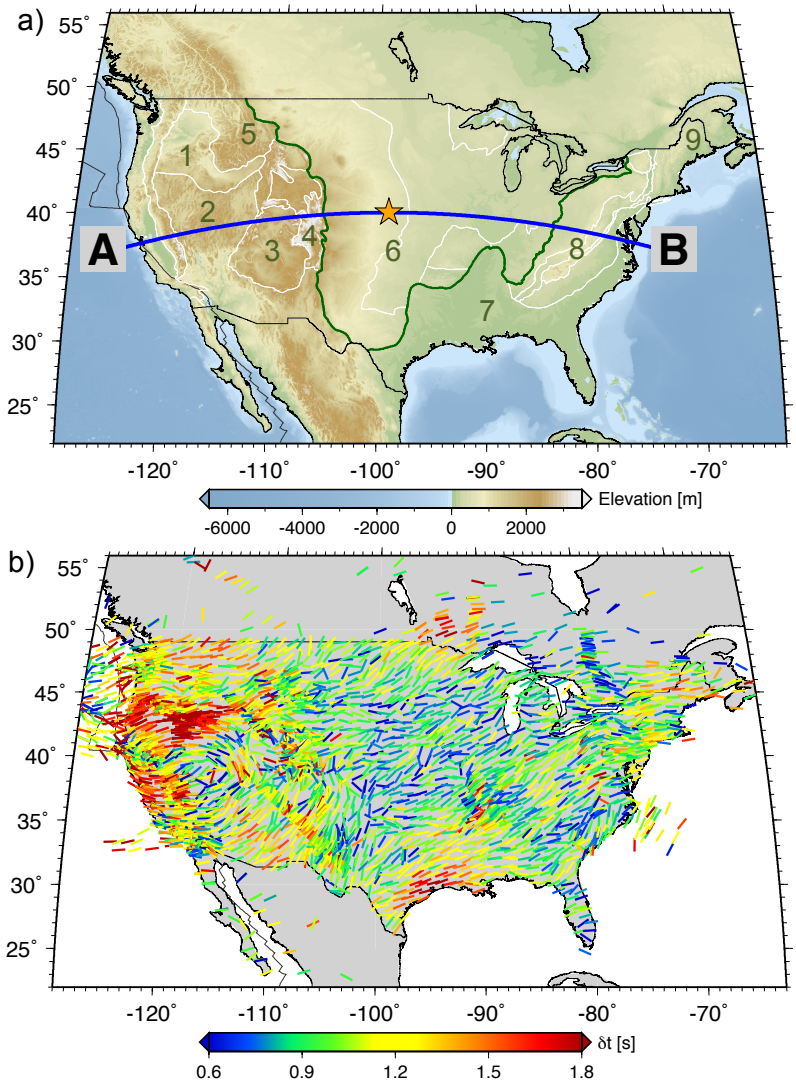

Figure 1: Study area showing topography and physio-graphic regions (a) and station-averaged shear-wave splitting measurements (b). In a), elevation is shown in the background; green lines are the orographic boundaries here used to define the western, central and eastern U.S.; white lines are the boundaries of different physio-graphic regions; blue profile shows the location of the cross section of the flow profiles discussed below. Main physio-graphic regions that are discussed in this paper are marked with numbers, they are: 1) Columbia Plateau, 2) Basin and Range, 3) Colorado Plateau, 4) Southern Rocky Mountains, 5) Northern Rocky Mountains, 6) Interior Plains, 7) Coastal Plains, 8) Appalachian Mountain Range, and 9) New England province. In b), fast orientation and delay times (δt) of the SWS measurement compilation are shown by stick orientation and color, respectively.

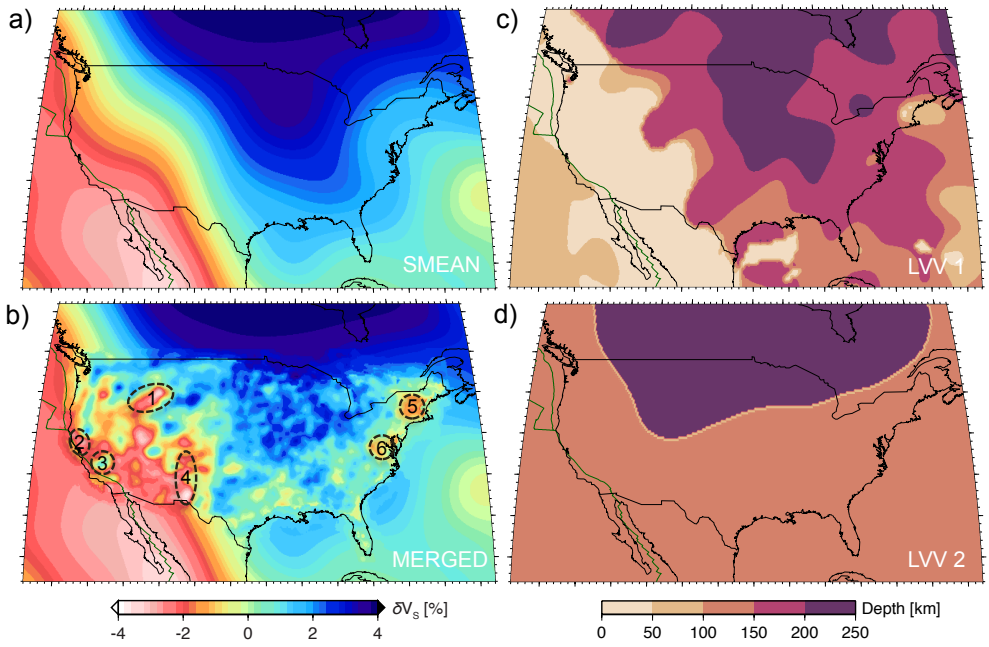

Figure 2: Tomography (a and b) and lithospheric thickness (c and d) models. Colors in a) and b) indicate S wave velocity anomalies (δV_S) for the SMEAN (Becker and Boschi, 2002) and MERGED (cf. Schmandt and Lin, 2014) tomography models, respectively, at 200 km depth. In plot b), the outlined features are upper mantle anomalies that are discussed in the result section, they are: 1). Yellowstone and Snake River Plain, 2). Salton Trough, 3). northern Great Valley, 4). Rio Grande Rift, 5). New England, and 6) central Appalachian. Colors in c) and d) show the inferred depth of the lithosphere in viscosity models LVV1 and LVV2, respectively.

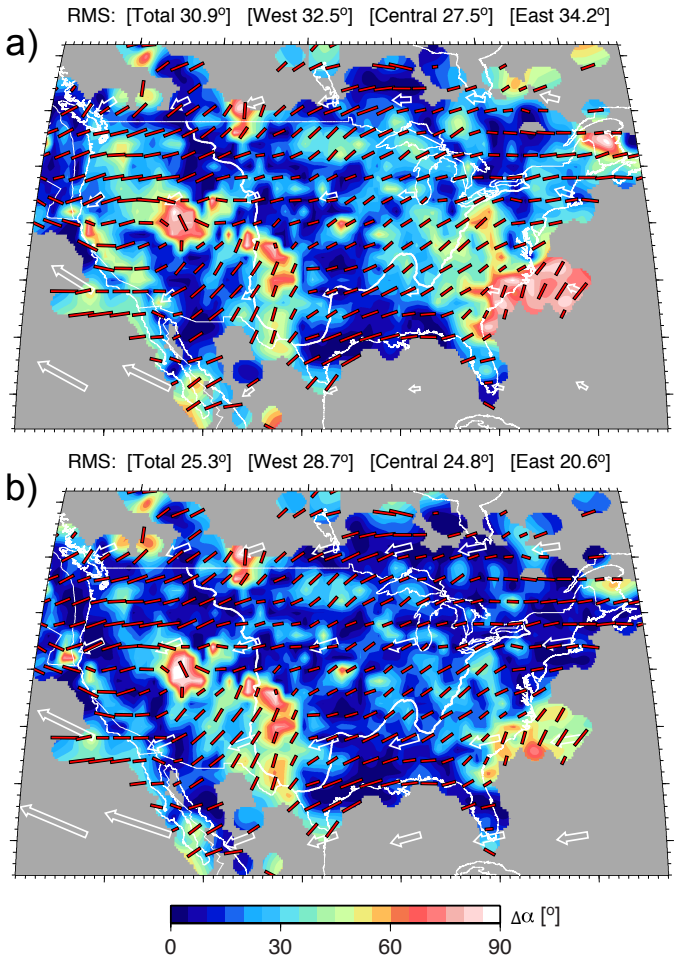

Figure 3: Absolute angular misfit ($\Delta\alpha$) between SKS splits and absolute plate motion (APM) orientations in the no-net-rotation (NNR) reference frame of Argus and Gordon (1991) (a), and in the spreading-aligned reference frame of Becker et al. (2015) (b). $2^\circ \times 2^\circ$ grid averaged SKS splits (based on Fig. 1b) are shown by red sticks. APM motions are indicated by white, open vectors. Background color indicates the value of $\Delta\alpha$, and title shows the map-wide and regional means of $\Delta\alpha$ for the sub domains indicated by heavy white lines, $\langle\Delta\alpha\rangle$.

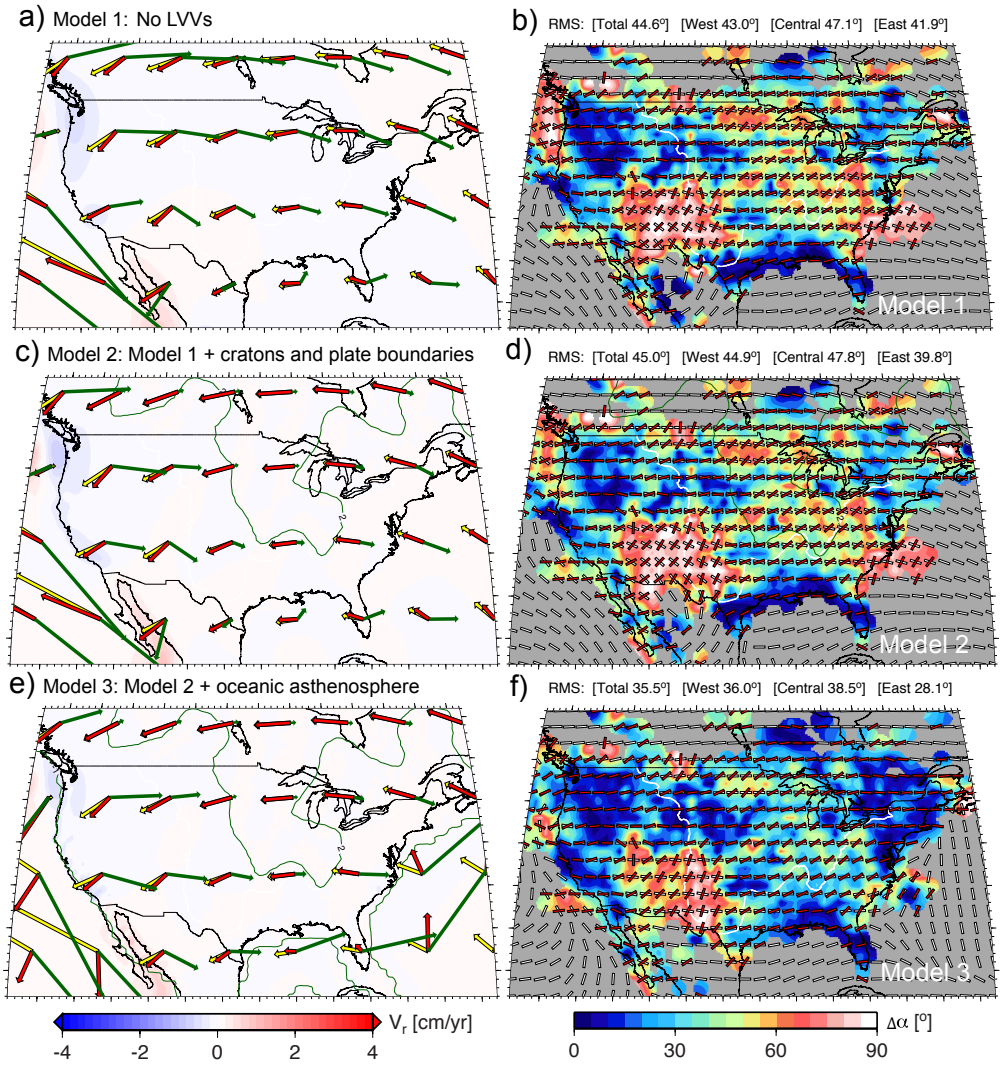

Figure 4: Upper mantle flow (a, c, and e) and the resulting angular misfit ($\Delta\alpha$) between SKS splits and flow-model predicted anisotropy (b, d, and f) of Models 1 (plate-induced shear, a and b), 2 (added cratons and weak zones, c and d), and 3 (added oceanic weak asthenosphere, e and f). In plot a), c), and e), radial flow is shown in background coloring (upwelling positive); surface velocities, flow at 200 km depth, and their vector difference (amplified by 5) are indicated by yellow, red and green vectors, respectively. In plot b), d), and f), $\Delta\alpha$ is shown in the background; SWS observed and flow model predicted SWS fast orientations depicted by red and white vectors, respectively. Title for b), d), and f) shows mean angular misfits as in Fig. 2.

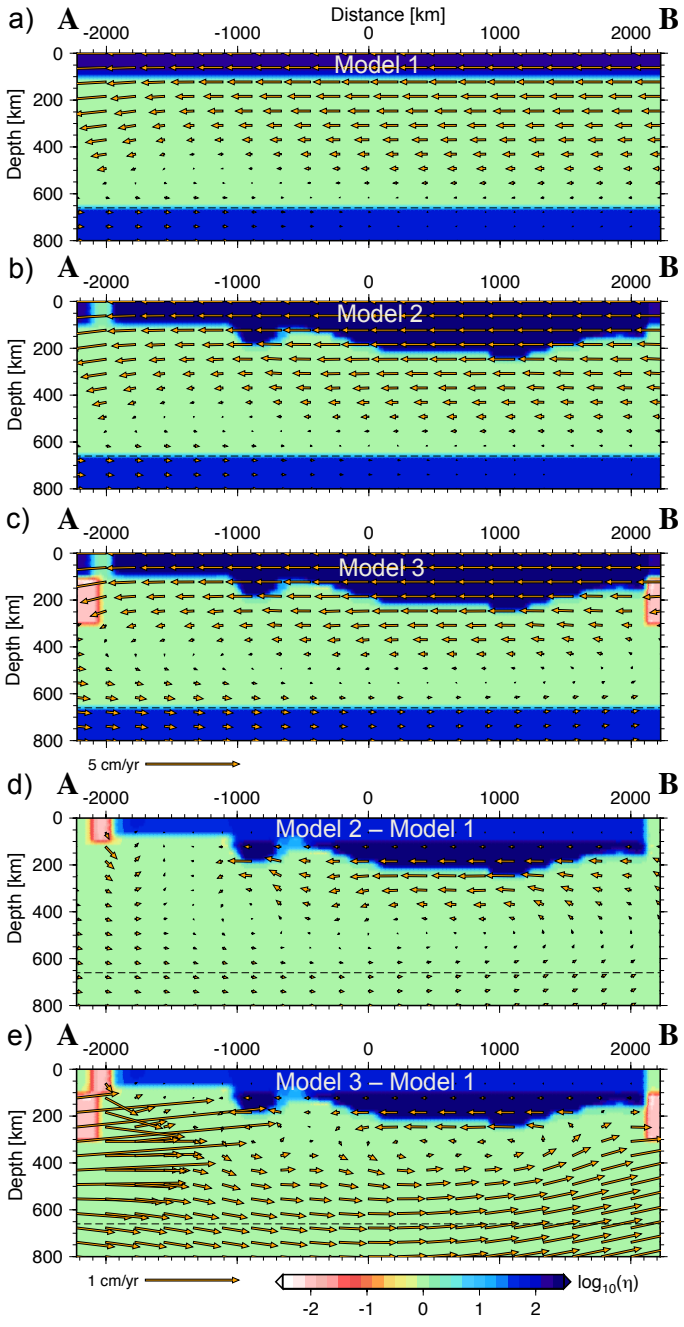

Figure 5: Cross-section of mantle flow for Models 1 (a), 2 (b), and 3 (c) along the profile shown in Fig. 1a. Background color shows the decadic logarithm of the upper mantle normalized viscosity. and orange vectors show flow velocity with the length scale shown beneath the bottom left corner of plot c). Sub-plots d) and e) show the differences in flow field and viscosity between Models 1 and 2 (d), and between Models 1 and 3 (e). Length scale of the differential flow vectors is shown beneath plot e).

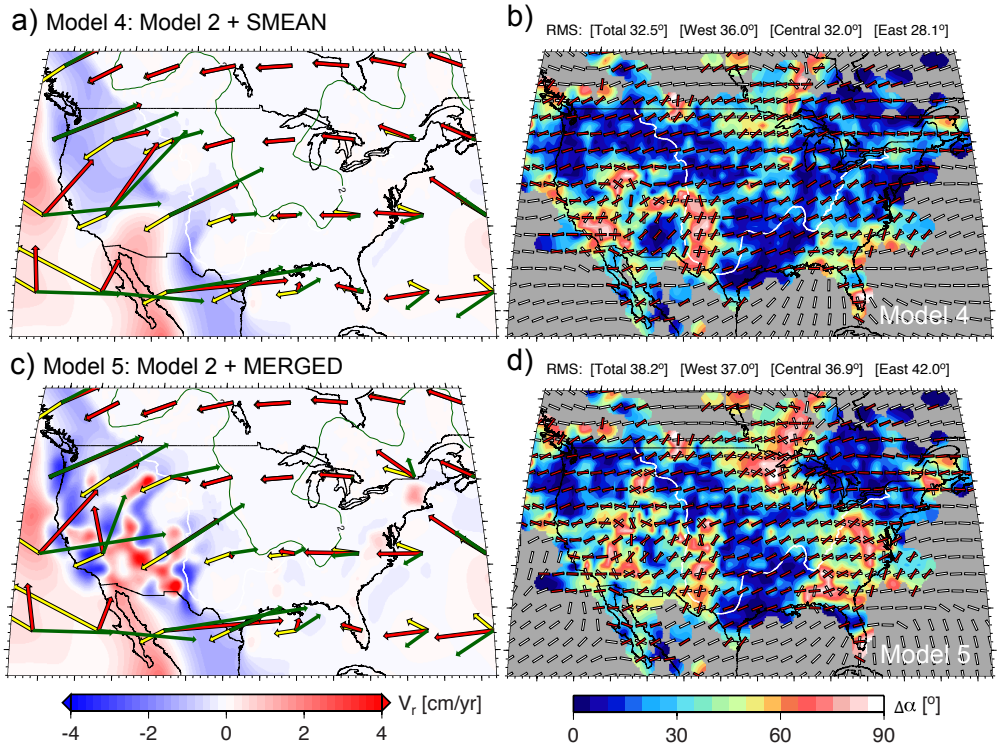

Figure 6: Effect of density anomalies. Flow field at 200 km depth (a and c) and the resulting $\Delta\alpha$ between SKS splits and flow predicted anisotropy (b and d) of Model 4 (SMEAN density driven flow, a and b) and 5 (MERGED density, c and d). See Fig. 4 for details.

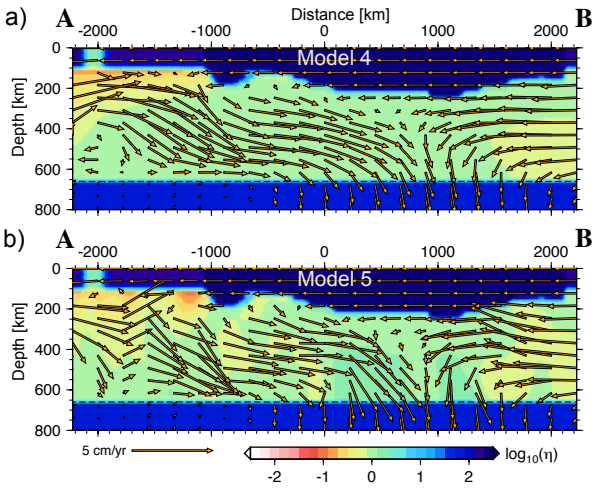

Figure 7: Velocity and viscosity profiles for Models 4 (a) and 5 (b). Scale of velocity vector length is shown beneath plot b). See Fig. 5 for details.

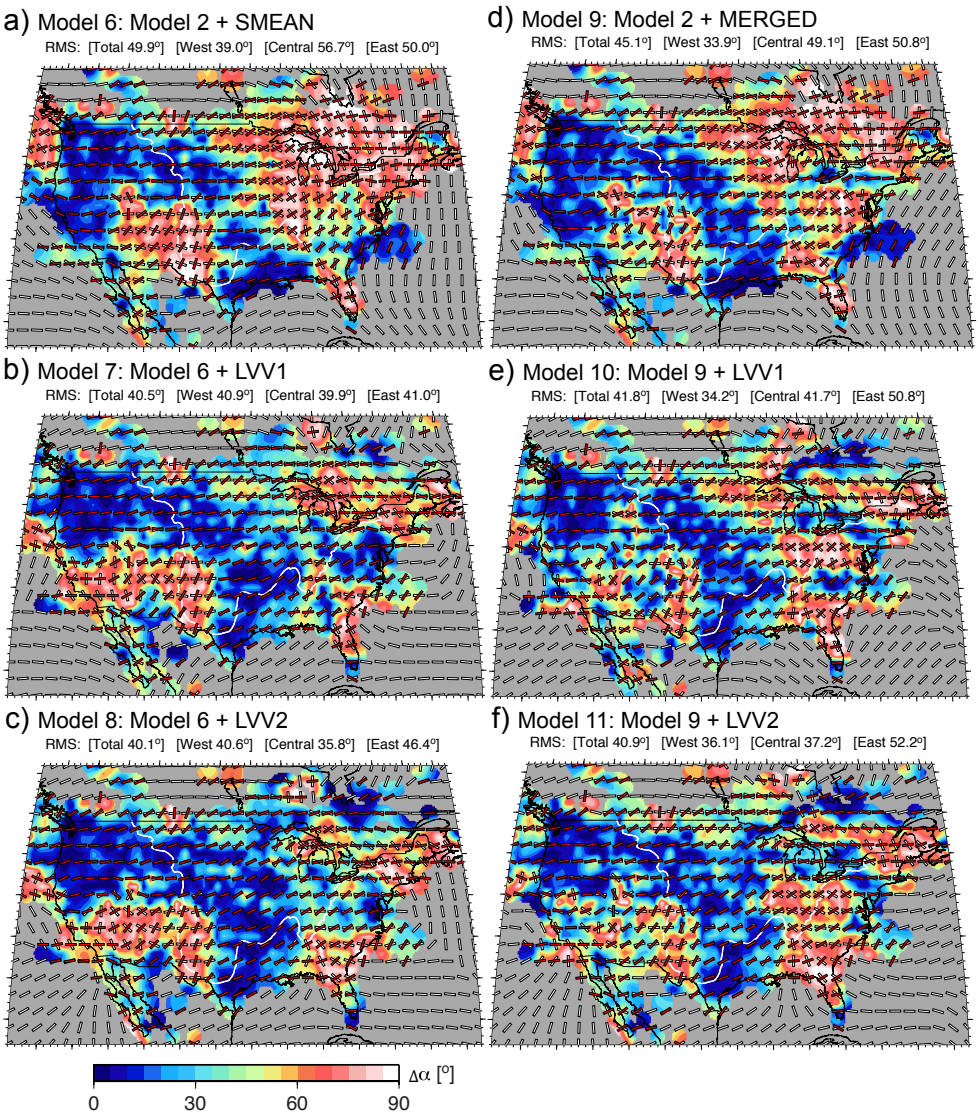

Figure 8: Effect of lateral viscosity variations. $\Delta\alpha$ between SKS splits and flow-model predicted anisotropy of Models 6 (a), 7 (b), 8 (c), 9 (d), 10 (e), and 11 (f). See Fig. 4 for details.

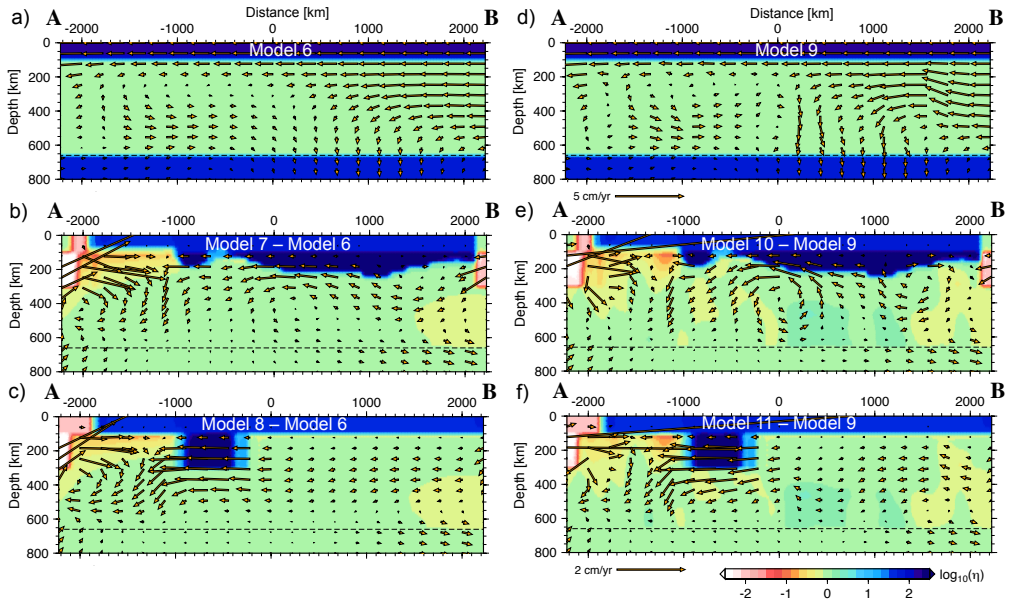

Figure 9: Flow profiles of Models 6 (a) and 9 (f) with velocity vector length scale shown beneath plot f). Plots c), e), h) and j) show the differences in velocities and viscosity between Models 7 and 6 (c), Models 8 and 6 (e), Models 10 and 9 (h), and Models 11 and 9 (f). Differential velocity vector length scale is shown beneath plot j). See Fig. 5 for details.

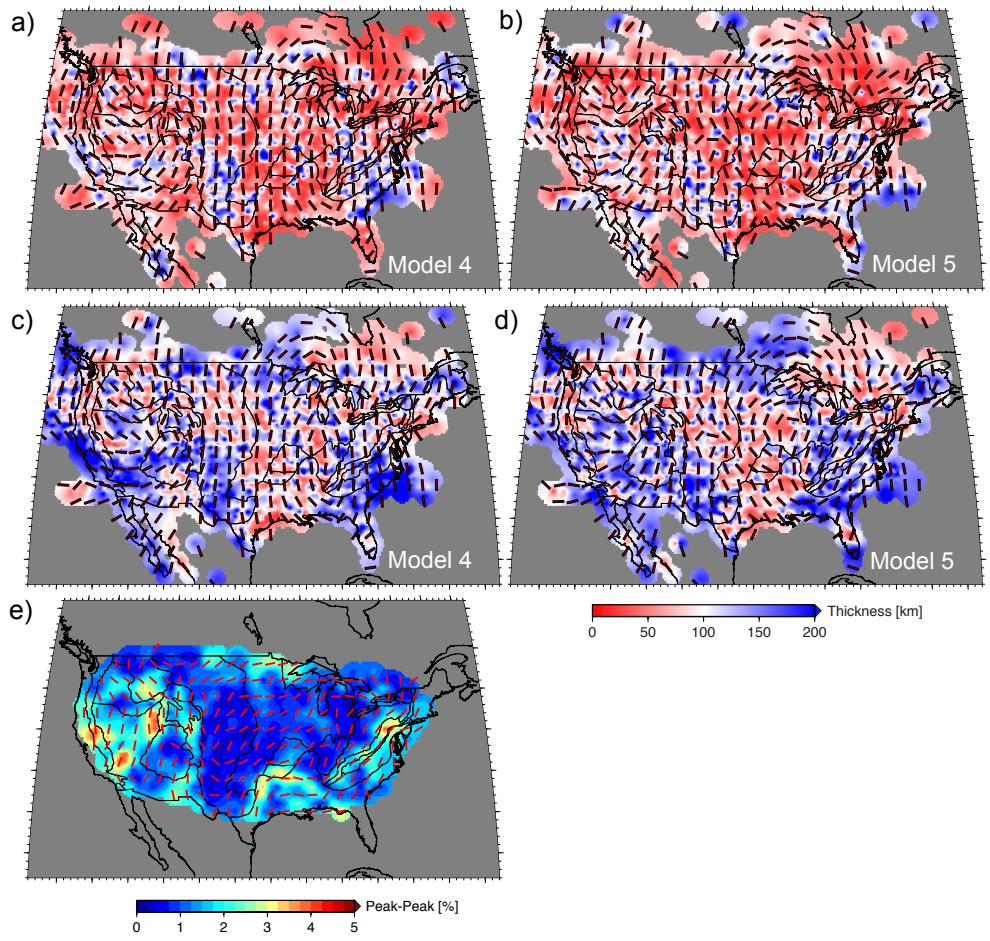

Figure 10: Inferred lithospheric anisotropy resulting from matching Models 4 (a and c) and 5 (b and d) flow-predicted anisotropy to the SWS dataset. Plots a and b are results for using Tensor 1, and plots c and d for Tensor 2. In plots a, b, c, and d, the dark red vectors show the fast orientations of lithospheric complement, and the background color shows the equivalent thickness of the lithospheric complement layer. Plot e) shows the crustal azimuthal anisotropy determined by Lin and Schmandt (2014) for comparison. Red vectors show the $2^\circ \times 2^\circ$ grid averaged fast orientations, and the background color shows the peak to peak amplitude.